Applied Physics Letters ARTICLE scitation.org/journal/apl

Split-well direct-phonon terahertz quantum cascade lasers

Cite as: Appl. Phys. Lett. **114**, 191102 (2019); doi: 10.1063/1.5089854
Submitted: 23 January 2019 · Accepted: 16 April 2019 ·
Published Online: 14 May 2019

Asaf Albo,[1,a)] Yuri V. Flores,[2] Qing Hu,[2] and John L. Reno[3]

AFFILIATIONS

[1]Faculty of Engineering, Bar-Ilan University, Ramat Gan 5290002, Israel
[2]Department of Electrical Engineering and Computer Science and Research Laboratory of Electronics, Massachusetts Institute of Technology, Cambridge, Massachusetts 02139, USA
[3]Center for Integrated Nanotechnologies, Sandia National Laboratories, MS 1303, Albuquerque, New Mexico 87185-1303, USA

[a)]asafalbo@gmail.com

ABSTRACT

We present a so-called "split-well direct-phonon" active region design for terahertz quantum cascade lasers (THz-QCLs). Lasers based on this scheme profit from both elimination of high-lying parasitic bound states and resonant-depopulation of the lower laser level. Negative differential resistance is observed at room temperature, which indicates that each module behaves as a clean 3-level system. We further use this design to investigate the impact of temperature on the dephasing time of GaAs/AlGaAs THz-QCLs.

Published under license by AIP Publishing. https://doi.org/10.1063/1.5089854

The highest temperature reported for a pulsed operation of terahertz quantum cascade lasers (THz-QCLs) is ∼200 K.[1] The major physical mechanism that limits the operating temperatures of THz-QCLs with the standard spatially vertical optical transition scheme is identified as the nonradiative thermally activated LO-phonon scattering from the upper to the lower laser level (LLL).[2] A strategy to counteract the temperature degradation of THz-QCLs is to reduce the thermally activated LO-phonon scattering rate by using spatially diagonal optical transitions.[3,4] Besides the LO-phonon scattering channel, THz-QCLs also suffer from thermally activated leakage of charge carriers into the continuum[5] or excited bound states.[6,7] Additional potential limiting mechanisms for the performance of THz-QCLs are thermal backfilling[8] and line broadening.[9]

In both resonant-phonon (RP)[10,11] and direct-phonon two-well (TW) schemes,[12,13] the phonon well is the widest in the structure. As such, a higher level in this well is not far above the upper laser level (ULL), so it provides a leakage channel at high temperatures. In order to suppress this leakage channel, we used a narrower phonon well,[6,14] which resulted in an energy separation of the lower laser level (LLL) and the ground state larger than the LO-phonon energy. This deviation from the resonance slows down the depopulation of the LLL.[6,14]

Here, we suggest and experimentally demonstrate a split-well direct-phonon (SWDP) scheme for THz-QCLs. A similar approach based on the RP-scheme was exploited in Refs. 15–17. As a result of this scheme, the lasers benefit from a more flexible design and an efficient isolation of laser levels from excited and continuum states. A clean three-level system, that is, most of the electrons reside in the three lowest subbands even at elevated temperatures, is achieved as indicated by the negative differential resistance (NDR) behavior at room temperature. Due to the enhanced flexibility in the design, these schemes serve as a good platform to study the mechanisms that govern the temperature performance of THz-QCLs.

In our scheme (Fig. 1), we use an intrawell thin barrier to control the energy splitting between the LLL (level 2 in the scheme) and the ground state (level 1 in the scheme). By adjusting the thickness of the intrawell barrier, we can change the energy separation to be the exact LO-phonon energy ($E_{21} = 36$ meV), enabling the fastest LO-phonon scattering rate depopulating the LLL. Additionally, the large interface roughness (IFR) scattering in our design may assist in depopulating the LLL even faster.[18–21] In previous designs,[6,14] we used thinner wells in order to push the excited states to higher energies that resulted in a trade-off—i.e., larger than the LO-phonon energy splitting ($E_{21} = 55$ meV)—which resulted in a longer LLL lifetime. In the design presented here, due to the thickness adjustability of the intrawell barrier, we push the excited states to higher energies while keeping the resonant LO-phonon scattering condition of $E_{21} = 36$ meV. In general, negative effects of slow LLL depopulation on the laser performance are evidenced for THz-QCLs in several works,[6,14,22–24] justifying the need to keep the fastest possible LLL depopulation rate.

As can be seen in Fig. 1, the structure is based on three subbands in each module (all other levels are considered parasitic), where the

Published under license by AIP Publishing

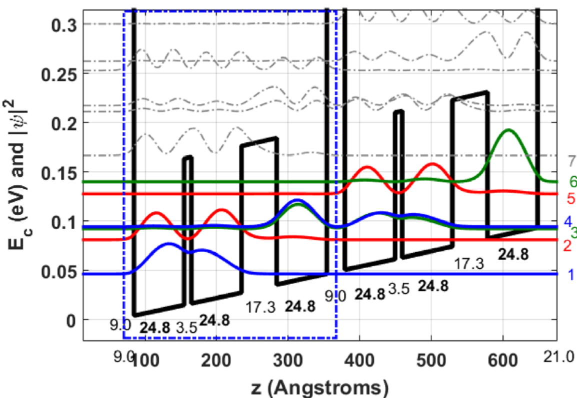

FIG. 1. Band diagram of two sequential periods termed "module i" (left, marked by a dashed-dotted box) and module i+1 (right) of the SWDP THz-QCLs with mixed barriers: $Al_{0.55}Ga_{0.45}As$ injection barrier (nominally pure AlAs barrier) and $Al_{0.15}Ga_{0.85}As$ radiative and intrawell barriers, corresponding to the energy levels of device VB0837 with a doping level of $\sim 3 \times 10^{10}$ cm^{-2}. More details regarding the design and the device parameters can be found in Tables I and II.

LLL (level 2 in the scheme) and the injector level of the following module (level 1 in the scheme) are aligned to form a direct phonon scattering scheme similar to that of the TW scheme.[8,12,13] One motivation for the new design here is to keep the direct-phonon scheme, which has several advantages over RP structures. It has very fast depopulation of the LLL solely by LO-phonon scattering (no resonant tunneling is involved), and is less sensitive to the misalignment of the laser levels due to the Poisson effect.[14,25] Additionally, the extra barrier of the SWDP further reduces carrier leakage channels, including (nonthermally activated) intermodule leakage.

Here, we investigate diagonal ($f \sim 0.25$) SWDP THz-QCLs with mixed potential barriers. The THz-QCL scheme of this study contains $Al_{0.55}Ga_{0.45}As$ injection barriers (nominally pure AlAs barriers), and the rest of barriers are with the standard composition of 15% aluminum, i.e., $Al_{0.15}Ga_{0.85}As$ (Fig. 1). The carrier density per cascade is $\sim 3 \times 10^{10}$ cm^{-2} and the MBE wafer is labeled VB0837. More details regarding the design, fabrication details, and device parameters can be found in Tables I and II.

Devices fabricated from VB0837 demonstrate a relatively high maximum operating temperature of $T_{max} \sim 170$ K (Fig. 2). The energy scheme in Fig. 1 shows that the three active subbands (levels 1–3) are well separated from excited states (level 7 and above). The first excited state (level 7) above the ULL (level 3) is spatially located in the next neighboring quantum well and energetically located about $\sim$73 meV above the ULL. As indicated visually by the scheme in Fig. 1, the spatial overlap of this excited state with the ULL is quite low. In addition, the first excited state (level 7) is also energetically positioned above the ULL of the second module (level 6) in the higher energy side of the scheme ("module i+1"). This suggests that nonthermally activated carrier leakage channels, including intermodule leakage, are further reduced in these structures as compared to the more standard designs in two-well structures.[14] A lasing frequency of $\sim$2.4 THz was observed (Fig. 2 inset) with respect to the designed lasing value of $\sim$3.65 THz. The device includes mixed barriers with a nominally thin AlAs injection barrier. If, instead of using ideally pure AlAs injection barriers, we assume the more realistic case of having *de-facto* wider AlGaAs barriers with a reduced aluminum composition, and consequently lower band edge discontinuity ($Al_{0.55}Ga_{0.45}As$ barriers); in fact, we can calculate the measured laser emission frequency of $\sim$2.4 THz. This therefore suggests that some amount of Ga-Al intermixing has to be present in the structure, reducing the conduction band of the nominally thin AlAs barriers. In the following, we work with the corrected (in the sense described before and also given in Tables I and II) values for layer thicknesses and conduction band offsets.

A relatively large interface roughness (IFR)-induced gain broadening is calculated for the SWDP design (Table II). However, the encouraging experimental result of $T_{max} \sim 170$ K demonstrates the potential of these structures.

In Fig. 3, the I-V curves show clean NDR behavior at low and room temperatures, indicating an effective isolation of the active three

TABLE I. Main nominal design parameters and device data.

Device	Lasing energy [meV]	E_{21} [meV]	Oscillator strength	Nom. expected activation energy [meV]	E_{47} [meV]	Layer sequence [#ML[a]], barrier composition, and doping level	Process details
Device VB0837 (Fig. 1)[b]	11.1	34.5	0.26	24.9	72.5	***9.0***/24.8/**3.5**/24.8/**17.3**/24.8 (24.8 underlined) 353 periods Total thickness 10 μm GaAs/mixed barriers ***$Al_{0.55}Ga_{0.45}As$ (Inj.)*** and **$Al_{0.15}Ga_{0.85}As$ (Rad., Intraw.)**	Metal-metal (100 Å Ta/2500 Å Au) Top contact n^{+} layer was removed and the bottom contact is 50 nm thick GaAs with a doping of 5×10^{18} cm^{-3}
						2.13×10^{16} cm^{-3} in the 24.8 ML wells (2.98×10^{10} cm^{-2}).	Dry etched Mesa size 150 μm $\times$ 1.8 mm

[a]#ML stands for the number of monolayers, where the "AlGaAs" barriers are given in "bold" and "bold-italics" (Injector barrier), and the GaAs wells in Roman; the doped layer in the sequence is underlined, and the barriers' composition and doping details are elaborated in the following lines.
[b]These calculations were conducted with an $Al_{0.55}Ga_{0.45}As$ injection barrier (and not the nominal pure AlAs barrier) in order to take into account the effect of intermixing between the AlAs injection barrier and the neighboring layers. Specifically, here, we take into account an averaged aluminum composition over a width that includes the AlAs width and the additional two monolayers on each side of the AlAs barrier.

Published under license by AIP Publishing

TABLE II. Device parameters and performance.

Device	Injection coupling ($2\hbar\Omega_{ij}$) [meV]	Design electric field [kV/cm]	τ^0_{ul} [ps][a]	τ^0_{21} [ps][b]	IFR gain broadening [meV][c]	Lasing energy [meV]	Expected activation energy [meV]	J_{th} (10 K) [A/cm^2]	J_{max} (10 K) [A/cm^2]	Dynamic range (10 K) [A/cm^2]	J_{max} (290 K) [A/cm^2]	T_{max} [K]
Device VB0837 (Fig. 1)[d]	2.08	16.5	1.21	0.18	4.37	10.05	25.5	578	928	350	750	170

[a]ULL to LLL raw LO-phonon scattering time.
[b]LLL (level 2) to injector (level 1) LO-phonon scattering time.
[c]Calculated according to Ref. 21.
[d]These calculations were conducted with an $Al_{0.55}Ga_{0.45}As$ injection barrier (and not the nominal pure AlAs barrier) in order to take into account the effect of intermixing between the AlAs injection barrier and the neighboring layers. Specifically, here, we take into account an averaged aluminum composition over a width that includes the AlAs width and the additional two monolayers on each side of the AlAs barrier.

laser states from excited and continuum states. The current of the higher-voltage side of the data decreases as the temperature increases. Specifically, the maximum current (J_{max}) decreases as the temperature increases even above the maximum lasing temperature, which cannot be explained by a decrease in the stimulated emission rate as in Ref. 26. The current of the lower voltage side of the data increases as the temperature increases. Both features will be explained later by increased level broadening, due to an increase in the dephasing rate as the temperature increases.

In Fig. 4(a), we present the threshold current vs temperature curve of the device with a relatively high characteristic temperature $T_o \approx 310$ K. In Fig. 4(b), we analyzed the light output power (P_{out}) vs temperature data. Activation energies (E_a) were extracted from the best fit to the data using Arrhenius plots according to the method in Ref. 2 using the formula $\ln\left(1-\frac{P_{out}(T)}{P_{out\,max}}\right) \approx \ln(a) - \frac{E_a}{kT}$, where a is a constant. We were able to extract a reasonable activation energy value for devices fabricated from VB0837 when ignoring the data for low temperatures and close to T_{max}. The data and values are presented in Fig. 4(b). The smoothness of the curve in the temperature range that was used for extraction justifies the validity of our procedure. In addition to output power, we also analyzed the current dynamic range (ΔJ_d) dependence on temperature. Activation energies for the current

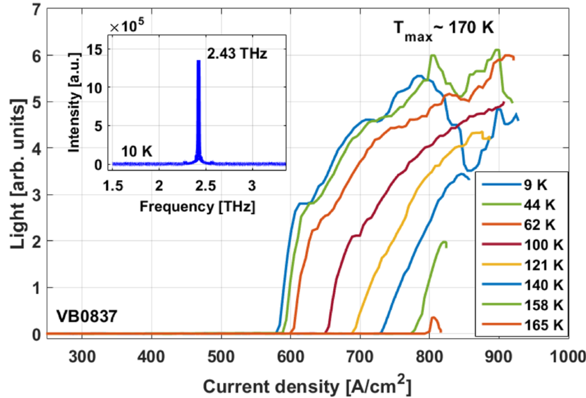

FIG. 2. Pulsed light-current measurements of device VB0837. More details on the structure can be found in Tables I and II and Fig. 1.

dynamic range $\Delta J_d = (J_{max} - J_{th})$ were extracted from the best fit to the data using Arrhenius plots according to $\ln\left(1-\frac{\Delta J_d(T)}{\Delta J_{d\,max}}\right) \approx \ln(b) - \frac{E_a}{kT}$, where b is a constant, similar to the procedure for the output power. The coincidence of the temperature dependence of ΔJ_d and $P_{out}(T)$ (below T_{max}) suggests that both the transport and emission processes are influenced by the same dynamics: stimulated emission within a module, and therefore intermodule leakage does not contribute significantly to the current density.

The experimental activation energy presented in Fig. 4(b) (~26 meV) is the expected value for thermally activated LO-phonon scattering, i.e., $E_{LO} - h\nu$. This result indicates an effective suppression of thermally activated leakage channels through excited states. Similar values are observed for both the lasing output power and the current dynamic range. Interestingly, the current dynamic range dependence on temperature data shows a smoother behavior and higher accuracy in the activation energy value than the data on the output power. The high temperature part of the data omitted from the fit of the lasing output power is attributed to the unstable laser transport characteristics at temperatures close to T_{max}. The somewhat "noisy" behavior of the measured L vs I characteristics in Fig. 2 at low temperatures and the lower slope in Fig. 4(b) at low temperatures are probably related to the high excess temperature of electrons below 100 K (the electron temperature is higher than the lattice temperature below 100 K).[2,25]

In Fig. 5, we plot J_{max} vs T all the way up to room temperature, which shows an interesting nonmonotonic behavior. In clean three-level devices, the temperature dependence of J_{max} provides important information. Transport through the injector barrier is described by the Kazarinov-Suris[27] formula for tunneling involving dephasing

$$J = eN \times \frac{2\Omega^2 \tau_{\parallel}}{4\Omega^2 \tau\tau_{\parallel} + \omega_{21}^2 \tau_{\parallel}^2 + 1}, \qquad (1)$$

where Ω is the coupling between the injector and the ULL subbands across the barrier, τ is the ULL lifetime, $\tau_{\parallel}$ is the decoherence (dephasing) time between the injector and the ULL subbands, and ω_{21} is the energy misalignment between the two. Equation (1) describes a Lorentzian centered at $\omega_{21} = 0$, with a width proportional to $\sqrt{4\Omega^2\tau\tau_{\parallel} + 1}$. The maximum current ($J_{max}$) is then given by

Published under license by AIP Publishing

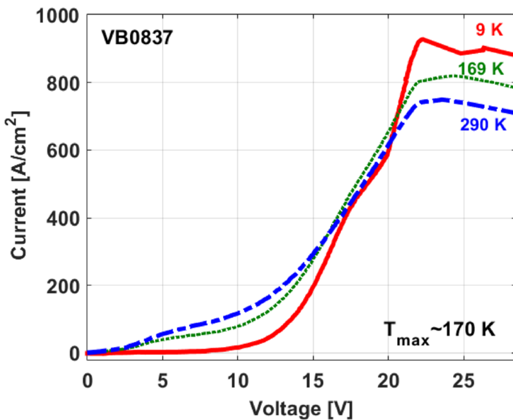

FIG. 3. Current-voltage curves of device VB0837 at low, around maximum operating, and room temperatures. The measured maximum operating (lasing) temperature (170 K) is indicated.

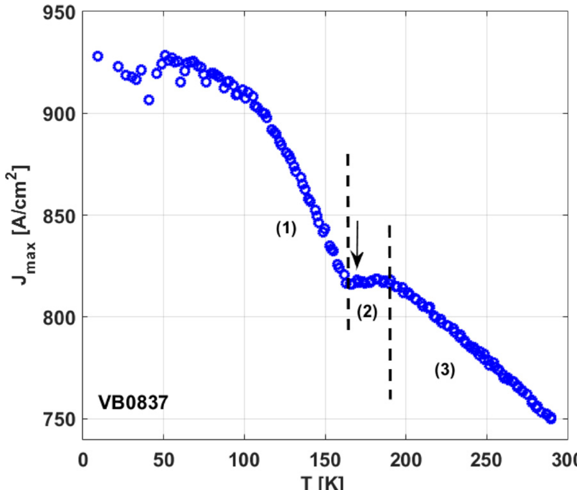

FIG. 5. Maximum current densities vs temperature of device VB0837 are given in blue circles. The three regions are defined in the text and the maximum operating temperatures T_{max}, (black arrow) are marked.

$J(\omega_{21}=0) = J_{max} = eN \times \frac{2\Omega^2\tau_\parallel}{4\Omega^2\tau\tau_\parallel+1}$. Transport limited by resonant tunneling (week-coupling regime) corresponds to the case where $\tau \ll \frac{1}{4\Omega^2\tau_\parallel}$ and $J_{max} = 2eN\Omega^2\tau_\parallel$, whereas the lifetime-limited transport (strong-coupling regime) corresponds to the opposite case $\tau \gg \frac{1}{4\Omega^2\tau_\parallel}$ and $J_{max} = \frac{eN}{2\tau}$.[26,28] In the latter regime—to which highly diagonal designs belong—stimulated emission can affect the transport due to the reduction of the ULL lifetime. As a consequence, for the maximum current density prior to the onset of NDR, J_{max} will decrease with temperature below T_{max} since $J_{max} \sim \frac{1}{\tau} \approx \frac{1}{\tau_{st}}$. The decreasing J_{max} reflects the reduction of the dynamic range as the temperature increases. When the lasing ceases above T_{max}, the maximum current will start to increase since $J_{max} \sim \frac{1}{\tau} \approx \frac{1}{\tau_{nr}}$, and the ULL lifetime is now dominated by the nonradiative lifetime τ_{nr} that decreses with the temperature. This behavior will continue up to the point where the current becomes limited by resonant tunneling (transition to the weak-coupling regime), where J_{max} will again decrease with T since now $J_{max} \sim \tau_\parallel$, and $\tau_\parallel$, the decoherence time between the injector and the ULL, decreases as the temperature increases. The identification and analysis of these three regions, i.e., (1) a strong-coupling regime under lasing conditions ($T < T_{max}$) in which τ is strongly influenced by stimulated emission, (2) a strong-coupling regime under nonlasing conditions ($T > T_{max}$), and (3) a weak-coupling regime, will shed some light on the behavior of our three-level system.

The results of the maximum current J_{max} vs temperature in Fig. 5 clearly identify the three regions defined above. For clearer identification of the regions described above, we mark the regions and T_{max} by a black arrow. From the decrease of J_{max}, as the temperature increases up to T_{max} ~170 K (region 1), it is clear that the transport under lasing is limited by the ULL lifetime. Above T_{max}, when the device stops to lase, the ULL-lifetime limited behavior continues as indicated by a slight increase in J_{max} as the temperature increases up to a temperature of ~190 K (region 2). Above this temperature (~190 K), J_{max} starts to decrease again as the temperature increases. This decreasing J_{max} is an indication of transport limited by resonant tunneling, in which the dephasing time decreases (and line broadens) as the temperature increases (region 3). This analysis shows experimentally that the dephasing time and the line broadening become more significant at high temperatures, consistent with earlier theoretical works,[9] which were previously accessible only by simulations.[9,21,29–31] For better performance, in future designs, one may increase the coupling strength of the injector and the ULL to widen the temperature range of the ULL-lifetime limited behavior (strong-coupling regime) to higher

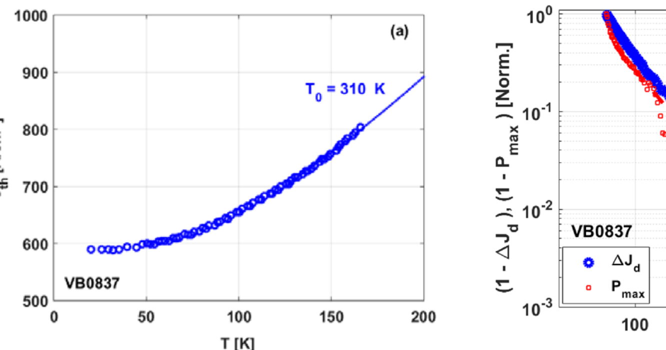

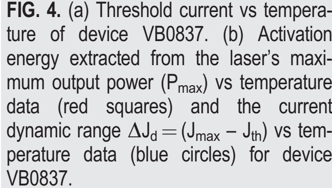
FIG. 4. (a) Threshold current vs temperature of device VB0837. (b) Activation energy extracted from the laser's maximum output power (P_{max}) vs temperature data (red squares) and the current dynamic range $\Delta J_d = (J_{max} - J_{th})$ vs temperature data (blue circles) for device VB0837.

Published under license by AIP Publishing

temperatures, in order to facilitate an effective tunneling injection at elevated temperatures.

In conclusion, we experimentally demonstrate a split-well direct-phonon (SWDP) scheme for THz-QCLs, which allows more flexible control of the carrier dynamics and efficient isolation of these laser levels from excited and continuum states. By keeping the depopulation of the LLL at the resonance, the design allowed us to investigate the effect of temperature on the dephasing time and the line broadening.

A. Albo would like to acknowledge the Israel Science Foundation (ISF) for their Grant No. 1556/18 and the Bar-Ilan University for their generous Starting Grant for New Faculty Members. Y. V. Flores would like to acknowledge the Research Fellowship Program of the German Research Foundation, DFG under Grant No. FL945/1-1. This work was supported by NSF, NASA, Israel MoD, and ISF. This work was also performed, in part, at the Center for Integrated Nanotechnologies, an Office of Science User Facility operated for the U.S. Department of Energy (DOE) Office of Science. Sandia National Laboratories is a multi-mission laboratory managed and operated by National Technology and Engineering Solutions of Sandia, LLC., a wholly owned subsidiary of Honeywell International, Inc., for the U.S. Department of Energy's National Nuclear Security Administration under Contract No. DE-NA-0003525.

REFERENCES

[1]U. S. Fathololoumi, E. Dupont, C. W. I. Chan, Z. R. Wasilewski, S. R. Laframboise, D. Ban, A. Matyas, C. Jirauschek, Q. Hu, and H. C. Liu, Opt. Express **20**(4), 3866 (2012).
[2]A. Albo and Q. Hu, Appl. Phys. Lett. **106**, 131108 (2015).
[3]S. Kumar, Q. Hu, and J. L. Reno, Appl. Phys. Lett. **94**, 131105 (2009).
[4]C. W. I. Chan, A. Albo, Q. Hu, and J. L. Reno, Appl. Phys. Lett. **109**(20), 201104 (2016).
[5]A. Albo and Q. Hu, Appl. Phys. Lett. **107**, 241101 (2015).
[6]A. Albo, Q. Hu, and J. L. Reno, Appl. Phys. Lett. **109**, 081102 (2016).
[7]D. Botez, S. Kumar, J. C. Shin, L. J. Mawst, I. Vurgaftman, and J. R. Meyer, Appl. Phys. Lett. **97**, 071101 (2010).
[8]B. S. Williams, S. Kumar, Q. Qin, Q. Hu, and J. L. Reno, Appl. Phys. Lett. **88**(26), 261101 (2006).
[9]R. Nelander and A. Wacker, Appl. Phys. Lett. **92**, 081102 (2008).
[10]B. S. Williams, H. Callebaut, S. Kumar, Q. Hu, and J. L. Reno, Appl. Phys. Lett. **82**, 1015 (2003).
[11]S. Khanal, L. Zhao, J. L. Reno, and S. Kumar, J. Opt. **16**, 094001 (2014).
[12]S. Kumar, C. W. I. Chan, Q. Hu, and J. L. Reno, Appl. Phys. Lett. **95**, 141110 (2009).
[13]G. Scalari, M. I. Amanti, C. Walther, R. Terazzi, M. Beck, and J. Faist, Opt. Express **18**(8), 8043 (2010).
[14]A. Albo, Y. V. Flores, Q. Hu, and J. L. Reno, Appl. Phys. Lett. **111**, 111107 (2017).
[15]S. Kumar, "Development of terahertz quantum-cascade lasers," Ph.D. thesis (Massachusetts Institute of Technology, 2007).
[16]R. W. Adams, K. Vijayraghavan, Q. J. Wang, J. Fan, F. Capasso, S. P. Khanna, A. Giles Davies, E. H. Linfield, and M. A. Belkin, Appl. Phys. Lett. **97**, 131111 (2010).
[17]C. W. I. Chan, Q. Hu, and J. L. Reno, Appl. Phys. Lett. **103**, 151117 (2013).
[18]J. B. Khurgin, Y. Dikmelik, P. Q. Liu, A. J. Hoffman, M. D. Escarra, K. J. Franz, and C. F. Gmachl, Appl. Phys. Lett. **94**(9), 091101 (2009).
[19]C. Deutsch, H. Detz, T. Zederbauer, A. M. Andrews, P. Klang, T. Kubis, G. Klimeck, M. E. Schuster, W. Schrenk, G. Strasser, and K. Unterrainer, Opt. Express **21**(6), 7209 (2013).
[20]M. Franckié, D. O. Winge, J. Wolf, V. Liverini, E. Dupont, V. Trinité, J. Faist, and A. Wacker, Opt. Express **23**(4), 5201 (2015).
[21]Y. V. Flores and A. Albo, IEEE J. Quantum Electron. **53**(3), 2300208 (2017); Erratum in Y. V. Flores and A. Albo, IEEE J. Quantum Electron. **53**(5), 9700101 (2017).
[22]A. Albo and Y. V. Flores, IEEE J. Quantum Electron. **53**(1), 2300105 (2017).
[23]M. Franckié, L. Bosco, M. Beck, C. Bonzon, E. Mavrona, G. Scalari, A. Wacker, and J. Faist, Appl. Phys. Lett. **112**, 021104 (2018).
[24]A. Albo and Y. V. Flores, IEEE J. Quantum Electron. **53**(5), 8500508 (2017).
[25]C. W. Ivan Chan, "Towards room-temperature terahertz quantum cascade lasers: Directions and design," Ph.D. thesis (Massachusetts Institute of Technology, 2015).
[26]I. Bhattacharya, C. W. I. Chan, and Q. Hu, Appl. Phys. Lett. **100**, 011108 (2012).
[27]R. F. Kazarinov and R. A. Suris, Sov. Phys. Semicond. **5**(4), 707 (1971).
[28]C. Sirtori, F. Capasso, J. Faist, A. L. Hutchinson, D. L. Sivco, and A. Y. Cho, IEEE J. Quantum Electron. **34**(9), 1722 (1998).
[29]H. Callebaut and Q. Hu, J. Appl. Phys. **98**, 104505 (2005).
[30]W. Freeman, J. Appl. Phys. **122**, 045701 (2017).
[31]R. L. Terazzi, "Transport in quantum cascade lasers," Ph.D. thesis (ETH Zurich, Zurich, Switzerland, 2012).

Published under license by AIP Publishing